

Supporting Information

Ultra-broadband hot-hole photodetector based on ultrathin gold film

Jun-Rong Zheng^{1‡}, En-Ming You^{1‡,}, Yuan-Fei Hu¹, Jun Yi^{1*} and Zhong-Qun Tian^{1*}*

¹State Key Laboratory of Physical Chemistry of Solid Surfaces, College of Chemistry and Chemical Engineering, School of Electronic Science and Engineering, Innovation Laboratory for Sciences and Technologies of Energy Materials of Fujian Province (iKKEM), Xiamen University, Xiamen 361005, China.

‡These authors contribute equally to this work

*Correspondence to: junyi@xmu.edu.cn; zqtian@xmu.edu.cn; emyou@xmu.edu.cn

1. Optical simulations

All optical simulations were carried out by Generalized Matrix Method¹ and further confirmed by finite element method (FEM) simulations using COMSOL Multiphysics. The optical constant of Al₂O₃², Si^{3, 4}, and bulk Au⁵ are obtained from the literature, respectively. The permittivity for ultrathin gold films is calculated by the Drude model,

$$\varepsilon = 1 - \frac{1}{\omega^2/\omega_p^2 + i\varepsilon_0\rho\omega} \quad (\text{S1})$$

where the plasma frequency ω_p and electrical resistivity ρ is obtained by fitting the experimental spectra from the literature⁶ (The results are shown in Table S1).

The absolute absorption intensity P_{abs} is calculated from the Ohmic loss in metal (The electric field of incident light is normalized to 1 V/m)

$$P_{\text{abs}}(z,\omega) = \frac{1}{2}\varepsilon(z,\omega)|E(z,\omega)|^2 \quad (\text{S2})$$

The absorptivity for ultrathin gold (gold reflector) is obtained is by integrating $P_{\text{abs}}(z,\omega)$ across its section and divided by the incident power.

Isolated 3 nm gold films were calculated first for comparison (Figure S1). Si was chosen to form the Schottky barrier with gold, also acting as a layer of anti-reflecting coating. Another layer of Al₂O₃ was also employed due to the relatively low refractive index and optical transparency in the desired wavelength range, which are beneficial for efficient anti-reflection^{7, 8}. The thicknesses of Al₂O₃ and Si were optimized to maximize the average absorptivity of gold film (Figure S2a). In addition, a cavity was used to further enhance the absorption of the device. From the perspective of taking into account absorption efficiency and band at the same time, we chose 80 nm as a compromise thickness for the bottom Si layer (Figure S2b, red dashed line).

Table. S1. Plasma frequency and electrical resistivity for ultrathin gold films with different thicknesses.

Thickness (nm)	$\rho (10^{-8} \Omega \cdot \text{m})$	$\omega_p (10^{16} \text{Hz})$
2	51.1	1.76
3	30.4	1.48
4	24.0	1.46
6	20.2	1.39
8	16.9	1.33
10	14.8	1.29

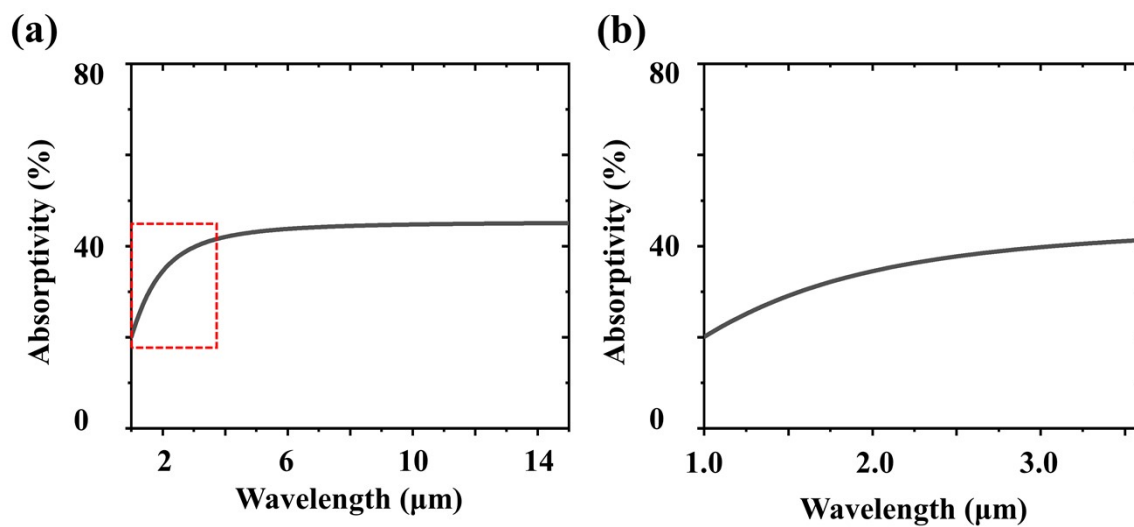


Fig. S1. (a) Absorption spectra of an isolated 3 nm gold film. (b) An enlarged view of the red box in (a).

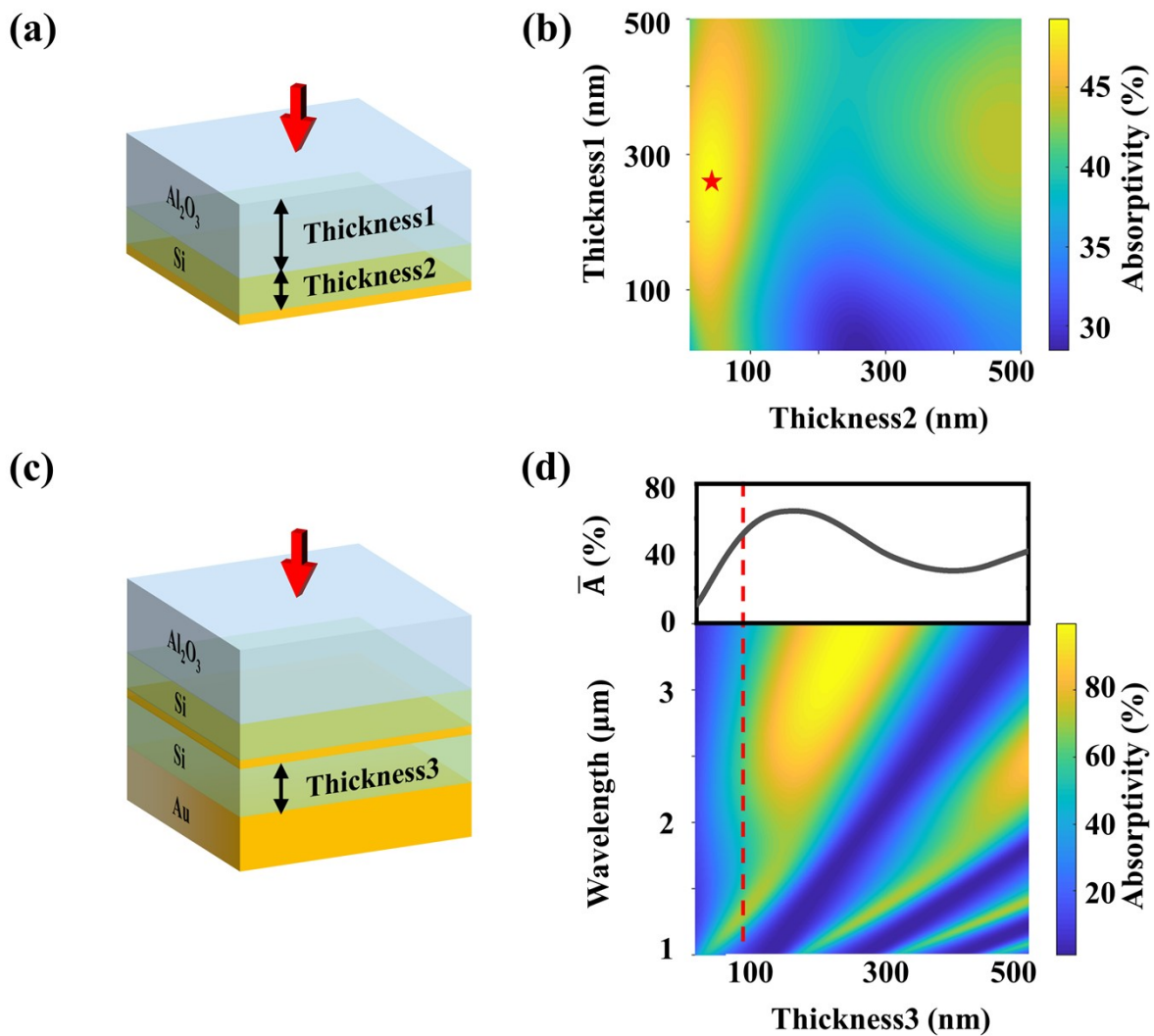


Fig. S2. The optimization process of each layer. (a) Schematics of the double-layer anti-reflecting coatings. (b) Average absorptivity as a function of the layer thickness of Si and Al₂O₃. The incident wavelength is from 1 μm to 3.6 μm. (c) Schematics of the Bragg mirror consisting of a Si layer and a thick gold mirror. (d) Average absorptivity as a function of the layer thickness of Si (upper) and the corresponding absorption spectrum (bottom)

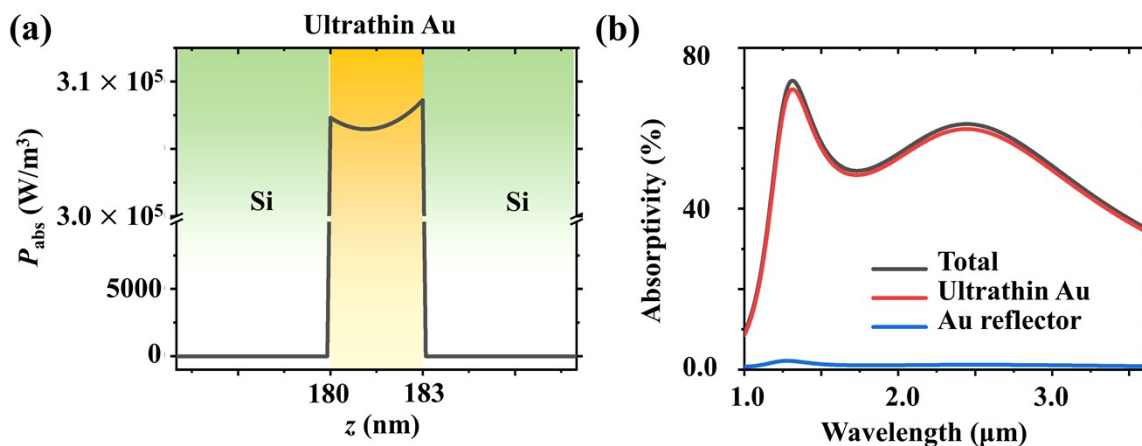


Fig. S3. (a) The distribution of absorption intensity P_{abs} in each layer at the wavelength of 1.3 μm . (An enlarged view of Fig. 1a near the ultrathin Au). (b) The total absorptivity of the device and the separated absorption from the ultrathin gold films and the bottom gold reflector.

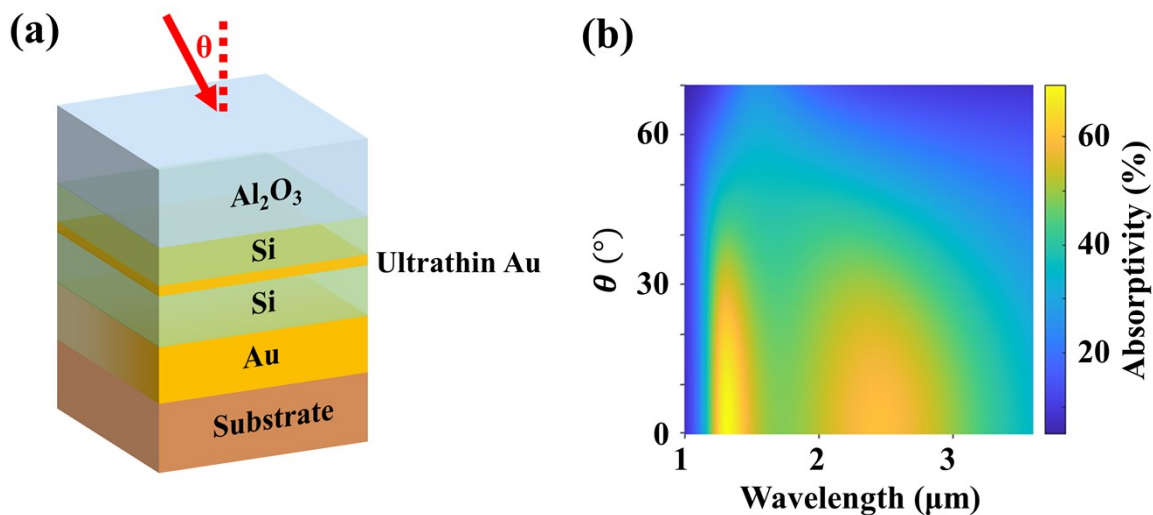


Fig. S4. (a) Schematic diagram of incident angle. (b) The total absorptivity of the device as a function of the incident angle and wavelength under TM illumination.

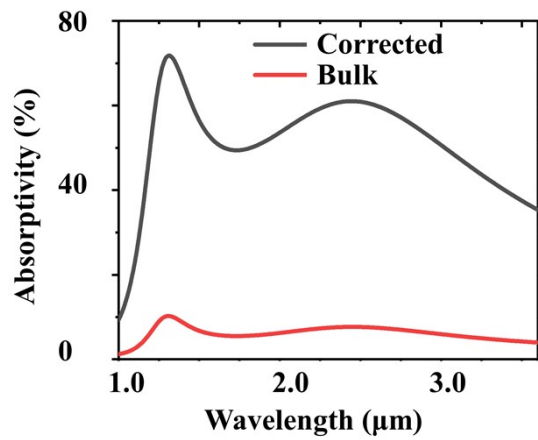


Fig. S5. The absorptivity of 3 nm Au device by using the permittivity of bulk gold and corrected data.

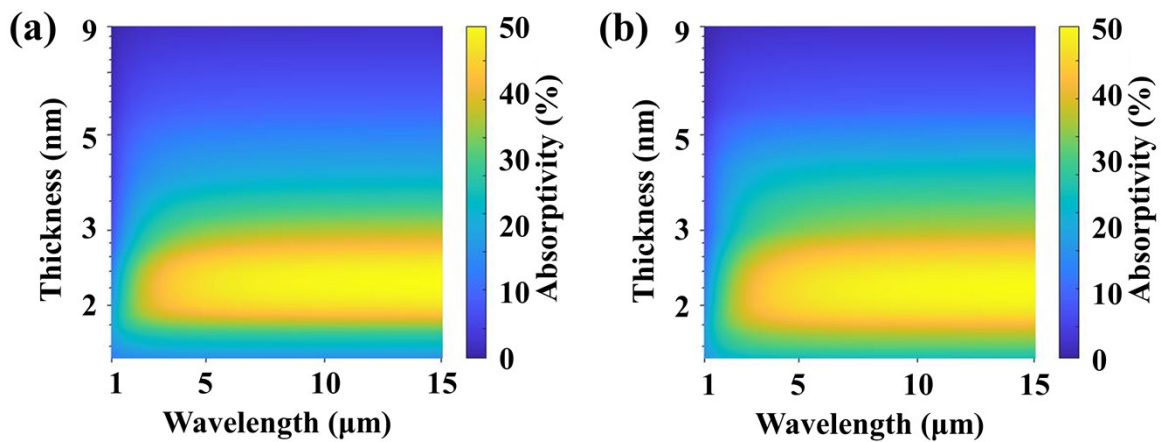


Fig. S6. The absorptivity of isolated (a) Au and (b) Ag films with different thicknesses. The resistivity for ultrathin Ag film is taken from literature⁹.

To consider the influence of spatial nonlocality of electrons in ultrathin metal films, we compared the absorption property of freestanding gold film with thickness of 3 nm by using either local (Drude) or nonlocal hydrodynamic models. In the nonlocal hydrodynamic model, the total electromagnetic fields $E(r,\omega)$ and current density $J(r,\omega)$ obey the following equations.

$$\nabla \times \nabla \times E(r,\omega) = \left(\frac{\omega}{c}\right)^2 \varepsilon_{core}(\omega) E(r,\omega) + i\omega\mu_0 J(r,\omega) \quad (\text{S3})$$

$$\frac{\beta^2}{\omega(\omega + i\gamma)} \nabla[\nabla \cdot J(r,\omega)] + J(r,\omega) = \frac{i\varepsilon_0\omega_p^2}{(\omega + i\gamma)} E(r,\omega) \quad (\text{S4})$$

where c , ε_0 and μ_0 are the speed of light, the permittivity and the permeability in vacuum, respectively. $\varepsilon_{core}(\omega)$ is the local permittivity of gold. γ and ω_p are the collision and plasmon frequencies of the Drude model for gold, which are extracted from the experimental data in ref¹⁰, $\gamma = 0.34 \text{ eV}$ and $\omega_p = 9.06 \text{ eV}$. β is the nonlocal parameter, which is related to the Fermi velocity of

gold, $v_F = 1.39 \times 10^6 \text{ m/s}$, as $\beta = \sqrt{\frac{3}{5}} v_F$. At the boundaries of the metal, an addition boundary condition $n \cdot J(r,\omega) = 0$ is applied, where n is the normal vector of the metal surface. The commercial software COMSOL Multiphysics based on finite element method (FEM) were employed to solve the partial differential equations.

Generally, for the thin film with surface structures which support localized plasmon resonance with significant local field enhancement, the nonlocal effect will lead to a blue shift of resonance energy. While for the ultrathin metal film used in our study is ideally flat and doesn't involve surface defects. As shown in Fig. S7a and b, the nonlocal effect shows little effect (deviations $< 0.02\%$) on the absorption property of ultrathin gold film under normal or oblique incidence (Fig. S7). However, when adding densely arranged hemispherical protrusions to the surface of flat film, the nonlocal effect should be counted in as larger deviations ($\sim 3.5\%$) appeared (Fig. S7c, d).

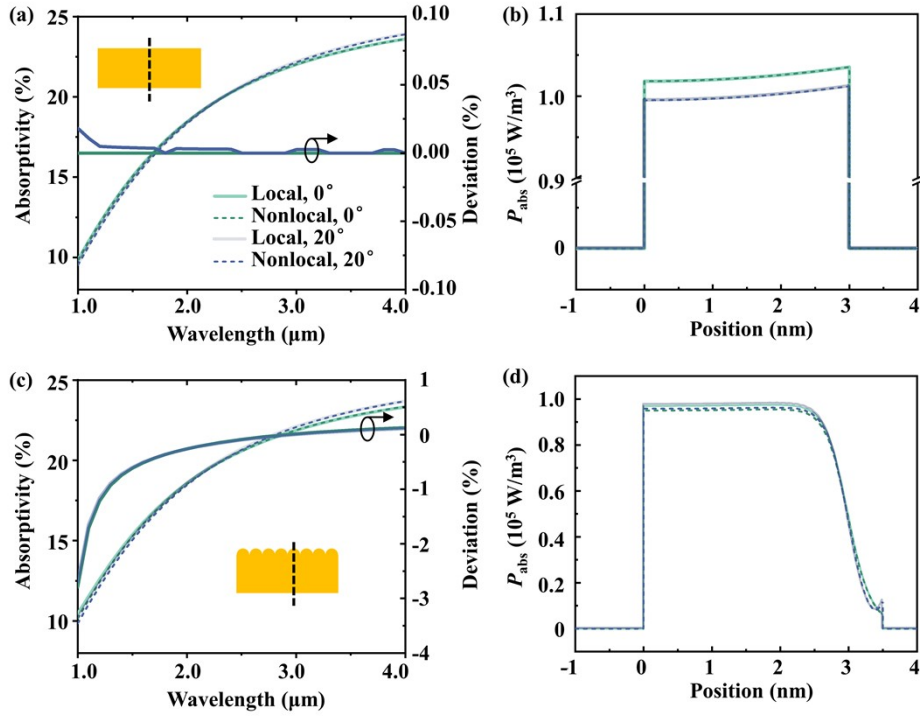


Fig. S7 (a) The absorptivity and (b) local absorption intensity distribution along the black dashed line in (a) of the freestanding gold film (3 nm) under different incident angle using either local or nonlocal model. (c) The absorptivity and (d) local absorption intensity distribution along the black dashed line in (c) of the freestanding gold film (3 nm) with densely arranged hemispherical protrusions (radius of 0.5 nm) under different incident angle using either local or nonlocal model.

2. Details about the transport process of hot carriers

In the main text, we assumed that L_{mfp} is in inverse proportion to the resistivity ρ in a certain material and define L_{mfp} for ultrathin gold by dividing the mean free path of bulk gold¹¹ by the multiple of ρ increase of ultrathin gold compared with bulk gold. The L_{mfp} for bulk gold is shown in Figure S7a. For 3 nm gold, the resistivity is $3.04 \times 10^{-7} \Omega \cdot \text{m}$, which is 13.8 times larger than that of bulk gold, the L_{mfp} shown in Figure 2 is divided by 13.8 from Figure S7a. The actual L_{mfp} of ultrathin gold films should be determined by experiment, which is not within the scope of this study.

To understand the effect of reduced free path quantitatively, we calculated the transported probability and the final photo response of the 3 nm gold-based device if one assumes that L_{mfp} is consistent with bulk gold, which shows that the reduced L_{mfp} leads to a decrease of only about 37% to the final responsivity (Figure S7d). This demonstrates that the reduced L_{mfp} does not destroy the transport process due to the several nanometers transport distance in our device.

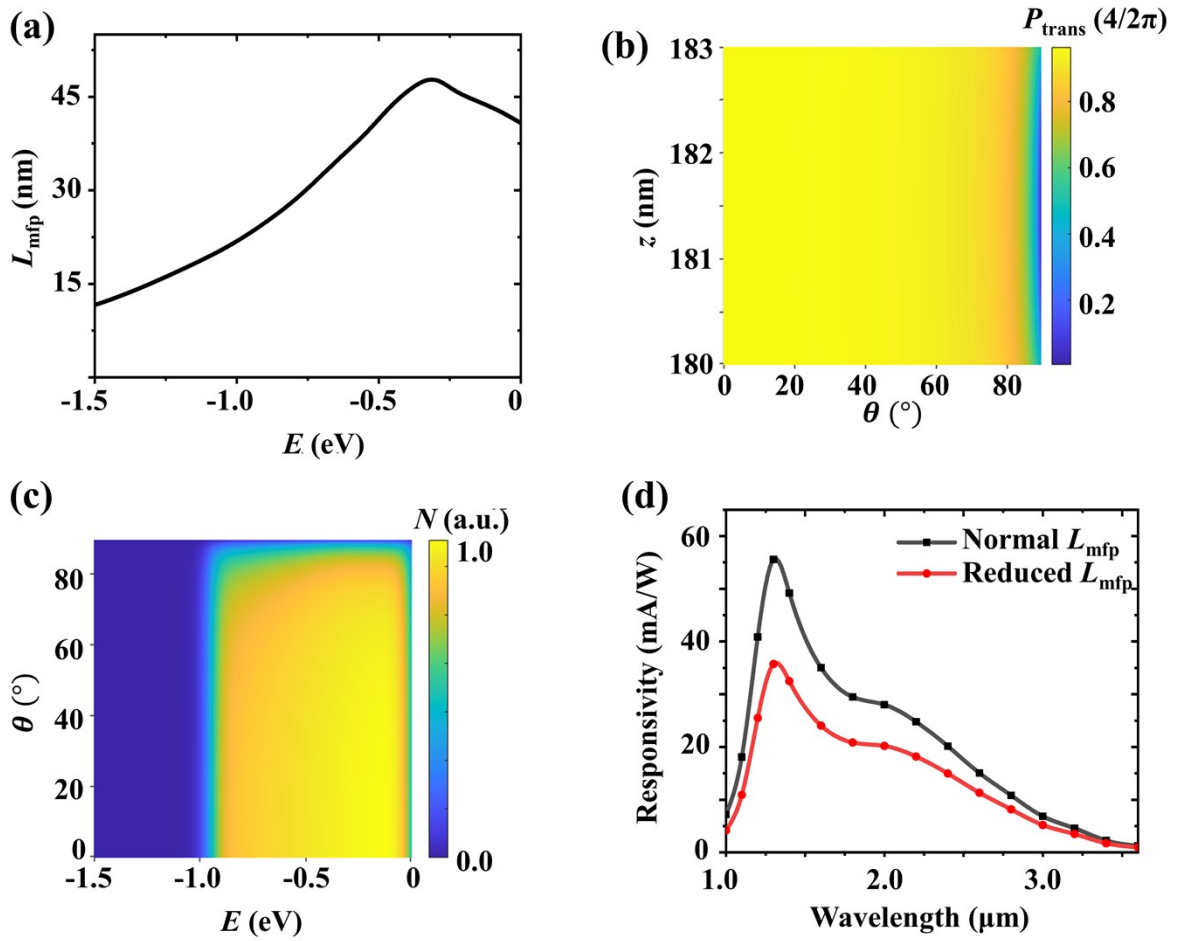


Fig. S8. Effect of reduced L_{mfp} to the 3 nm gold-based device. (a) The mean free path for bulk gold¹¹. (b) The position and angle distribution of P_{trans} at E of -0.5 eV by using normal L_{mfp} . (c) The energy and angle distribution of N for holes reaching the interface under the excitation of light with wavelength of $1.3 \mu\text{m}$ by using normal L_{mfp} . (d) The responsivity spectra were calculated by using normal L_{mfp} and reduced L_{mfp}

3. Details about the emission process of hot carriers

Obeying the parabolic free-carrier dispersion relation, the kinetic energy of electrons in metal or semiconductor is

$$E_{k,m} = \frac{\hbar^2}{2m^*}(k_m)^2 \quad (\text{S5})$$

$$E_{k,s} = E_{k,m} - \varphi_{SB} + V = \frac{\hbar^2}{2m^*}(k_s)^2 \quad (\text{S6})$$

where k_m and k_s is the momentum of holes in metal and semiconductor, φ_{SB} is the barrier height, V is the externally applied voltage.

The momentum mismatch of holes in the metal and semiconductor would cause reflection at the interface, the transmission probability is defined as

$$T = \frac{4\sqrt{(k_m^2 - k_x^2)(k_s^2 - k_x^2)}}{(\sqrt{k_m^2 - k_x^2} + \sqrt{k_s^2 - k_x^2})^2} \quad (\text{S7})$$

where k_x is the momentum component parallel to the interface, which is consistent in the both sides.

The dark current under a weak bias can be obtained from the thermionic emission theory¹²

$$J_d = AT^2 \exp\left(\frac{-q\varphi_{SB}}{k_B T}\right) \quad (\text{S8})$$

where A is the effective Richardson constant, T is the temperature, φ_{SB} is the barrier height, k_B is the Boltzmann constant and q is the elemental charge. For the combination of p-Si and Au, A and $q\varphi_{SB}$ are ~ 30 A/(cm²K²) and 0.32 eV, respectively, while for n-Si, they are ~ 110 A/(cm²K²) and 0.8 eV¹³. The detectivity D^* defined as $D^* = Res/\sqrt{2qJ_d}$ can be obtained subsequently (Fig. S9)

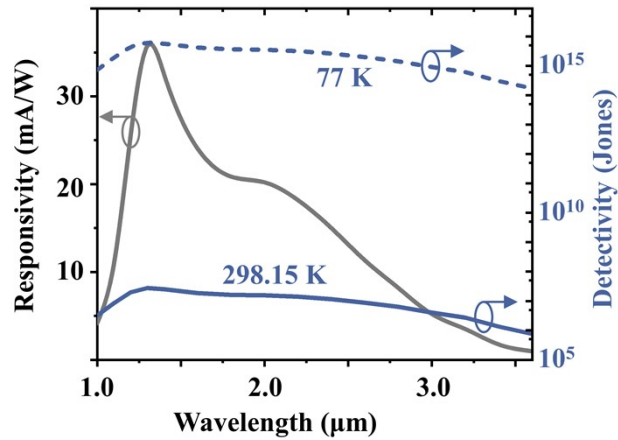


Fig. S9 The responsivity and detectivity spectrum of the proposed device under different temperature.

According to the entire process of the photocurrent generation, the response time may contain the following components: 1). Upon photo excitation, the excited carriers experience Landau damping ($1 \sim 100$ fs) and relaxation (100 fs ~ 1 ps) process to form Fermi-Dirac-like distribution¹⁴. 2). Then, it will take about a few femtoseconds for carriers' transportation to the metal/semiconductor interface (\sim nm) with Fermi velocity ($\sim 1 \times 10^6$ m/s for Au). 3). Part of carriers accomplish the interfacial electron transfer (emission) process and get into semiconductor (the time is hard to estimate). 4) The carriers in semiconductor collected by external circuit (transient process). However, the reported experimental response time of hot carrier photodetectors is on the order of millisecond¹⁵⁻¹⁷, which is possibly due to the poor time resolution of test equipment (sampling rate on the order of kHz) or other potential contribution not considered in the model.

References:

1. E. Centurioni, *Appl. Opt.*, 2005, **44**, 7532-7539.
2. R. L. Kelly, *J. Opt. Soc. Am.*, 1972, **62**, 1336-1336.
3. H. H. Li, *J. Phys. Chem. Ref. Data*, 1980, **9**, 561-658.
4. C. Schinke, P. C. Peest, J. Schmidt, R. Brendel, K. Bothe, M. R. Vogt, I. Kroger, S. Winter, A. Schirmacher, S. Lim, H. T. Nguyen and D. MacDonald, *AIP Adv.*, 2015, **5**, 067168.
5. R. L. Olmon, B. Slovick, T. W. Johnson, D. Shelton, S.-H. Oh, G. D. Boreman and M. B. Raschke, *Physical Review B*, 2012, **86**, 235147.
6. N. Luhmann, D. Hoj, M. Piller, H. Kahler, M. H. Chien, R. G. West, U. L. Andersen and S. Schmid, *Nat Commun*, 2020, **11**, 2161.
7. H. K. Raut, V. A. Ganesh, A. S. Nair and S. Ramakrishna, *Energy Environ. Sci.*, 2011, **4**, 3779-3804.
8. A. S. Sarkın, N. Ekren and Ş. Sağlam, *Sol. Energy*, 2020, **199**, 63-73.
9. D. Martinez-Cercos, B. Paulillo, R. A. Maniyara, A. Rezikyan, I. Bhattacharyya, P. Mazumder and V. Pruneri, *ACS Appl. Mater. Interfaces*, 2021, **13**, 46990-46997.
10. R. A. Maniyara, D. Rodrigo, R. Yu, J. Canet-Ferrer, D. S. Ghosh, R. Yongsunthon, D. E. Baker, A. Rezikyan, F. J. García de Abajo and V. Pruneri, *Nat. Photonics*, 2019, **13**, 328-333.
11. A. M. Brown, R. Sundararaman, P. Narang, W. A. Goddard and H. A. Atwater, *ACS Nano*, 2016, **10**, 957-966.
12. P. Berini, A. Olivieri and C. Chen, *Nanotechnology*, 2012, **23**, 444011.
13. S. M. Sze and K. K. Ng, *Physics of Semiconductor Devices*, John Wiley & Sons, Inc., New Jersey, 2006.
14. M. L. Brongersma, N. J. Halas and P. Nordlander, *Nat. Nanotechnol.*, 2015, **10**, 25-34.
15. B. Feng, J. Zhu, B. Lu, F. Liu, L. Zhou and Y. Chen, *ACS Nano*, 2019, **13**, 8433-8441.
16. S. L. Shinde, S. Ishii and T. Nagao, *ACS Appl. Mater. Interfaces*, 2019, **11**, 21965-21972.
17. S. Ishii, S. L. Shinde, W. Jevasuwan, N. Fukata and T. Nagao, *ACS Photonics*, 2016, **3**, 1552-1557.